

IMMEDIATE COMMUNICATION OPEN



The schizophrenia risk gene C4 induces pathological synaptic loss by impairing AMPAR trafficking

Rhushikesh A. Phadke¹, Alison Brack¹, Luke A. Fournier², Ezra Kruzich², Mingqi Sha², Ines Picard², Connor Johnson², Dimitri Stroumbakis², Maria Salgado², Charlotte Yeung², Berta Escude Velasco², Yen Yu Liu² and Alberto Cruz-Martin^{1,2,3,4,5}✉

© The Author(s) 2024

Neuroimmune interactions play a significant role in regulating synaptic plasticity in both the healthy and diseased brain. The complement pathway, an extracellular proteolytic cascade, exemplifies these interactions. Its activation triggers microglia-dependent synaptic elimination via the complement receptor 3 (CR3). Current models of pathological complement activity in the brain propose that accelerated synaptic loss resulting from overexpression of C4 (C4-OE), a gene associated with schizophrenia, follows this pathway. Here, we report that C4-mediated cortical hypoconnectivity is CR3-independent. Instead, C4-OE triggers impaired GluR1 trafficking through an intracellular mechanism involving the endosomal protein SNX27, resulting in pathological synaptic loss. Moreover, C4 circuit alterations in the prefrontal cortex, a brain region associated with neuropsychiatric disorders, were rescued by increasing neuronal levels of SNX27, which we identify as an interacting partner of this neuroimmune protein. Our results link excessive complement activity to an intracellular endo-lysosomal trafficking pathway altering synaptic plasticity.

Molecular Psychiatry (2025) 30:796–809; <https://doi.org/10.1038/s41380-024-02701-7>

INTRODUCTION

The complement cascade is central to neuroimmune interactions, playing a crucial role in synapse elimination and plasticity [1–3]. This pathway is a key player in innate immunity, where it forms a proteolytic protein cascade that clears debris, enhances inflammation, and tags pathogens for engulfment or destruction [4]. However, mice deficient in various members of the complement pathway exhibit aberrant connectivity patterns. For example, Stevens et al. showed that KO mice for either complement component 1q (C1q), the initiating protein in the pathway, or for the downstream effector protein complement component 3 (C3), exhibit deficits in connectivity in the visual thalamus [3]. Complement component 4 (C4A or just C4) is highly associated with schizophrenia (SCZ) such that specific structural variants and regulatory regions increase the expression of the gene and confer greater risk for this devastating disease [5]. C4 has been implicated not only in complex biological diseases like SCZ but also in normal development [6] and aging [7], neurodegenerative disorders [8, 9], and a higher risk for severe COVID-19 [10].

We and others have previously demonstrated that increasing the levels of the mouse and human homologs of C4 led to pathological synaptic loss in medial prefrontal cortex (mPFC) pyramidal neurons and PFC-associated behavioral deficits in mice [6, 11, 12]. Although microglia-dependent circuit refinement and activation of the CR3 is linked to increased complement activity in the brain, other non-glia mechanisms that could regulate synaptic plasticity or accelerate synaptic loss in pathological states have been largely unexplored [1, 3, 13].

Major contributors to synaptogenesis are dendritic filopodia, which are thin, specialized postsynaptic structures that orchestrate synapse formation by dynamically sampling potential presynaptic partners, thus optimizing circuit wiring [14, 15]. Our group [11] and others [6] have shown that specific deficits in filopodia function and a reduction in the fraction of gained dendritic spines, respectively, are observed with increased levels of C4. Indeed, C4 is expressed at low levels in cortical neurons and their synapses, potentially influencing intracellular signaling pathways [11]. Although it remains to be determined, this suggests that overexpression of C4 (C4-OE) might lead to synaptic loss, in part, through disruption in synaptic formation and spinogenesis, which are associated with changes in the recycling of glutamate receptors (GluRs) and long-term potentiation (LTP) [16–19].

Because of the known function of the complement pathway in immune defense, it is thought that in the nervous system, extracellular complement activity modifies synaptic plasticity in the healthy and diseased brain. In this model, astrocytes, microglia, and neurons, which are cellular sources of complement proteins [20–23], release complement proteins to the extracellular space, where they activate the pathway and the CR3 in microglia. However, recent studies in the immune system have discovered an intracellularly active complement pathway [24], which regulates metabolic pathways that control immune cell activity. As the vertebrate nervous and immune systems bear intriguing similarities [25], and cortical neurons in the mouse are a cellular source of C4, these results raise the possibility that in the brain,

¹Molecular Biology, Cell Biology & Biochemistry Program, Boston University, Boston, MA, USA. ²Neurobiology Section in the Department of Biology, Boston University, Boston, MA, USA. ³Department of Anesthesiology, University of Colorado Anschutz Medical Campus, Aurora, CO, USA. ⁴NeuroTechnology Center (NTC), University of Colorado Anschutz Medical Campus, Aurora, CO, USA. ⁵Neuroscience Graduate Program, University of Colorado Anschutz Medical Campus, Aurora, CO, USA.

✉email: alberto.cruzmartin@cuanschutz.edu

Received: 8 November 2023 Revised: 15 August 2024 Accepted: 16 August 2024

Published online: 3 September 2024

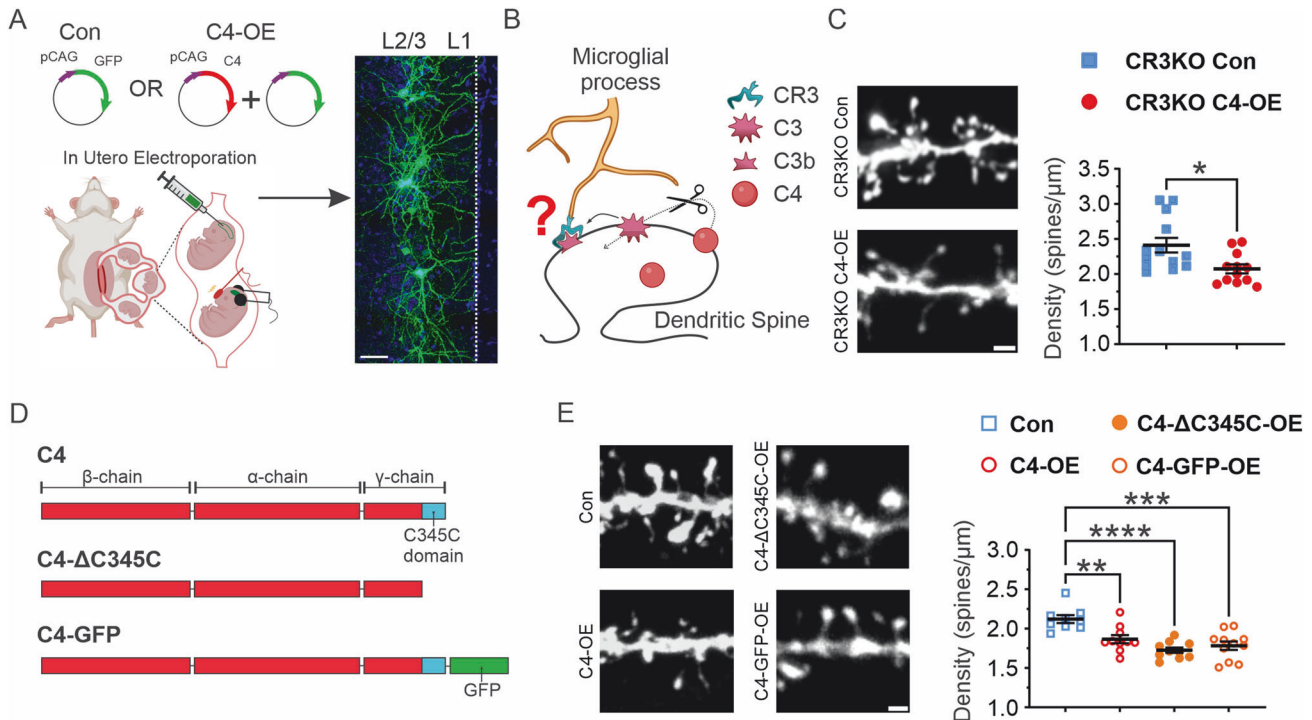


Fig. 1 C4 overexpression led to mPFC pyramidal neuron hypoconnectivity through a CR3-independent mechanism. **A** Left: In utero electroporation (IUE) procedure performed on E16 embryos. GFP-control (Con) represents the transfection of a single plasmid (GFP under the CAG promoter), while C4-OE represents the transfection of two plasmids (GFP and C4, both under the CAG promoter). Right: Representative 60X confocal image of P21–23 L2/3 mPFC neurons transfected with GFP (green). DAPI, cytoarchitecture. White dotted line, pia. Scale bar = 100 μm. **B** The model depicts the mechanism of spine removal through C3b recognition by the microglia expressing CR3 [54, 77]. **C** Left: Representative confocal image (60X) of CR3KO-control and CR3KO C4-OE. GFP, white signal. Scale bar = 2 μm. Right: C4-OE in mice lacking the CR3 (red circles) showed decreased dendritic spine density relative to control CR3KO mice (blue squares). *t*-test. **p* < 0.05. **D** Structure of wt C4 and C4 mutants (C4-ΔC345C and C4-GFP). C4 comprises three main chains [27] (β, α and γ) and a highly conserved C-terminal domain known as C345C [27] (cyan). **E** Left: Representative confocal image (60X) of Control and C4 mutants. Right: OE of wt C4 and mutants C4-GFP-OE and ΔC345C-OE caused a decrease in dendritic spine density relative to GFP-control. Cells were filled with mRuby3 instead of GFP for analysis of the C4-GFP-OE condition. One-way ANOVA. ***p* < 0.01, ****p* < 0.001, *****p* < 0.0001. Scale bar = 2 μm. **C** *N* = 13 CR3KO-control dendrites, 3 animals; *N* = 12 CR3KO-C4-OE dendrites, 3 animals, **E** *N* = 9 GFP-control dendrites, *N* = 10 C4-OE and C4-ΔC345C-OE dendrites, *N* = 11 C4-GFP dendrites, 3 animals each. All graphs, Mean ± SEM.

complement proteins, and specifically C4, regulate synaptic function through undiscovered intracellular mechanisms.

Here, we demonstrate that C4-OE leads to dendritic spine loss independent of the main phagocytic receptor CR3. Consistent with increased levels of this neuroimmune gene causing synaptic loss independent of complement activation, overexpression of C4 mutants that lack the enzymatic activity of the C3 convertase resulted in decreased connectivity compared to GFP-controls. Using a combination of in utero electroporation (IUE), biochemical and electrophysiological approaches, and stimulated emission depletion (STED) super-resolution nanoscopy, we put forward a new model of intracellular C4 action leading to disruption of AMPA GluR trafficking at the postsynapse, through an intracellular mechanism involving the endosomal trafficking protein SNX27 resulting in pathological synaptic loss. Our findings connect excessive complement levels to a pathway that alters synaptic plasticity within the intracellular endo-lysosomal recycling system.

RESULTS

C4 overexpression led to mPFC pyramidal neuron hypoconnectivity through a CR3-independent mechanism

To determine whether CR3 is necessary for C4-induced synaptic loss, we overexpressed C4 (C4-OE) via in utero electroporation (Fig. 1A) in transgenic mice lacking this key phagocytic receptor (CR3KO) of the complement cascade [2, 26] (Fig. 1B). Our group previously showed that we can reliably increase levels of C4 in

cortical synapses in vivo using IUE without dramatically altering the intrinsic electrophysiological properties of transfected cortical cells or inducing toxicity [11]. Remarkably, we observed approximately 16% reduction in the density of postsynaptic apical dendritic spines of layer (L) 2/3 cortical pyramidal neurons of postnatal (P) 21–23 mice as compared to GFP-controls, suggesting that C4 acts through a CR3 independent, non-canonical mechanism to drive synaptic loss (Fig. 1C).

Consistent with C4-OE causing synaptic loss independent of complement activation, overexpression of C4 mutants that lack the enzymatic activity of the C3 convertase—an enzyme essential for the generation of CR3 ligand (C3b)—by either the addition of a sterically large GFP tag (C4-GFP) or by deletion of the C345C domain (C4-ΔC345C) [27] (Fig. 1D) resulted in an approximately 22% decrease in spine density (Fig. 1E), compared to GFP-control mice. Therefore, C4-induced synaptic loss is independent of the activation of the downstream complement cascade.

SNX27 interacts with C4 and is essential for normal dendritic spine formation of L2/3 PFC neurons

Next, we leveraged the protein interactome (BioPlex), a comprehensive resource that maps protein interactions in human cells, to identify sorting nexin 27 (SNX27) as a potential intracellular interacting partner of C4 [28], which we validated for mouse homologs of the proteins by performing a co-immunoprecipitation (co-IP) assay in HEK293T cells (Fig. 2A) transfected with C4 and FLAG-tagged SNX27. SNX27 is an endosomal protein that recycles

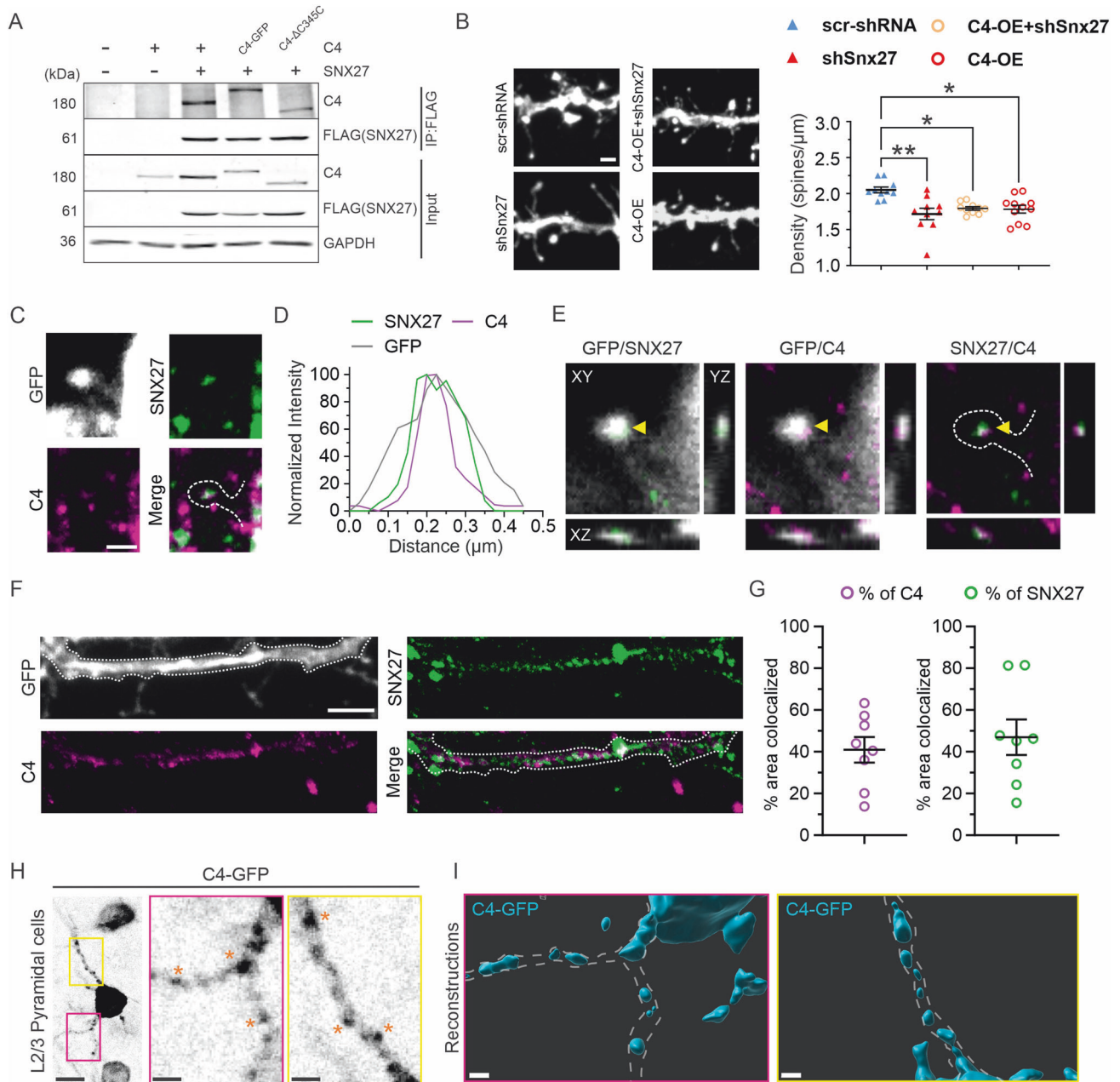
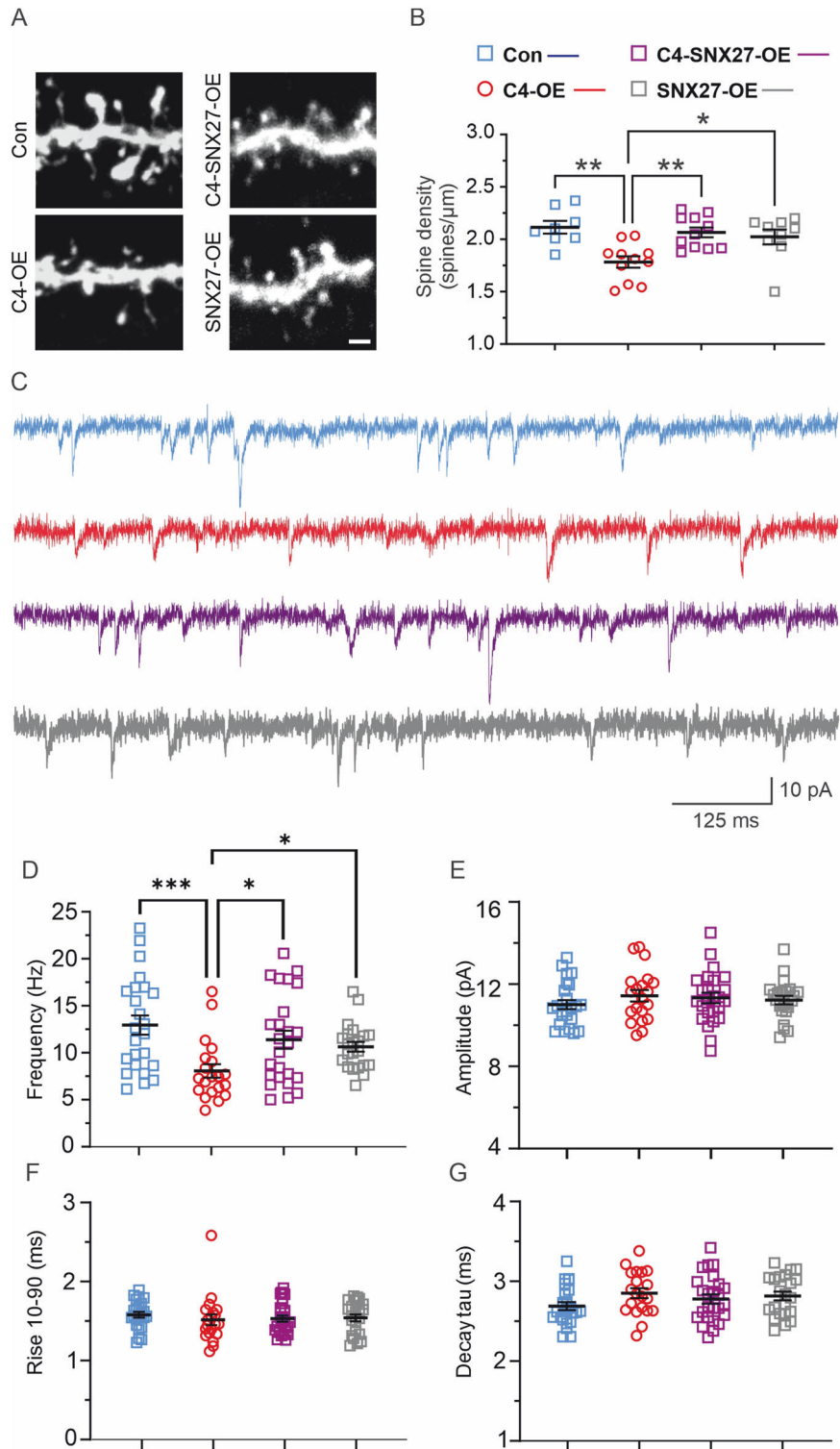


Fig. 2 SNX27 interacts with C4 and is essential for normal dendritic spine formation of L2/3 PFC neurons. **A** Western blot (WB) showing co-IP from HEK293T cells transfected with SNX27 and either C4, C4- Δ C345C or C4-GFP plasmids. The presence of proteins was detected by Western blotting in cell lysates (Input). Interaction of wt C4 and C4 mutants with SNX27 was detected by Western blotting of co-IP against FLAG-tagged SNX27 (IP: FLAG). Protein molecular weights, kilodaltons (kDa). + indicated the presence of wild type protein. **B** Left: Representative confocal image (60X) of scr-shRNA control (solid blue triangles), shSNX27 (solid red triangles), C4-OE + shSnx27 (orange open circles) and C4-OE (red open circles). GFP, white signal. Scale bar = 2 μm . Right: SNX27 KD and C4-OE + SNX27 KD led to a decrease in spine density relative to scr-shRNA to the same levels as C4-OE. One-way ANOVA. * $p < 0.05$, ** $p < 0.01$. **C** Representative STED images (60X) showing GFP-positive dendritic spine (white), SNX27 (green) and C4 (magenta) of DIV 14 cultured PFC neurons. White dotted line indicates spine morphology. Scale bar = 0.5 μm . **D** Normalized intensity profile of a line drawn through a spine head with SNX27 and C4 colocalized clusters in **(A)** showing intensities of GFP (gray line), SNX27 (green) and C4 (magenta). **E** Orthogonal views of **(C)** are shown (XY, YZ and XZ). Yellow arrowhead, SNX27 and C4 colocalization in the spine. **F** Representative STED images (60X). White dotted line, dendritic morphology. Scale bar = 2 μm . **G** Analysis C4 and SNX27 signals showed that approximately 41% of C4 area colocalized with SNX27 and approximately 44% of SNX27 area colocalized with C4 in spines and dendrites. **H** Representative confocal image (40X) of C4-GFP signal in electroporated L2/3 neurons. Scale bar = 15 μm . Boxes outlined by magenta and yellow show zoomed-in views of the insets, respectively. Scale bar = 5 μm . **I** 3D surface reconstructions of the insets in magenta and yellow, respectively, from **(H)**. Scale bar = 2 μm . **B** $N = 10$ scr-shRNA control, shSnx27 and C4-OE + shSnx27 dendrites, $N = 11$ C4-OE dendrites, 3 animals each. All graphs, Mean \pm SEM. **F**, **G** $N = 7$ dendritic segments, from 3 cells. All



glutamatergic AMPA receptors (AMPA) to the postsynaptic surface [29–31], strengthening synapses via LTP [32]. We also found that C4-GFP and C4- ΔC345C both bind to SNX27, suggesting that C4 mutants with disrupted C3 convertase activity do not interfere with C4-SNX27 interactions and C4 synaptic deficits are independent of the complement pathway (Fig. 2A). Using IUE and shRNA technology, we knocked down (KD) endogenous *Snx27* in mPFC neurons resulting in an approximately 20% decrease in spine density compared to the scrambled (scr)-shRNA control (Fig. 2B),

mimicking the C4-OE synaptic phenotype that we saw in vivo. Additionally, simultaneous knockdown (KD) of *Snx27* and overexpression of C4 (C4-OE + shSNX27) did not further reduce spine density compared to the C4-OE condition (Fig. 2B), suggesting a shared downstream pathway for these processes.

To determine whether C4 and SNX27 were likely to interact in neurons, we used stimulated emission depletion (STED) nanoscopy in dissociated mouse mPFC neuronal cultures (DIV 21) overexpressing C4 and FLAG-tagged SNX27. Using this approach,

Fig. 3 Increasing neuronal levels of SNX27 rescued the C4 hypoconnectivity phenotype. **A** Representative confocal image (60X) of GFP-positive P21–23 L1 apical tufts in GFP-control (Con, blue squares), C4-OE (red circles), C4-SNX27-OE (purple squares) and SNX27-OE (gray square) in the mPFC. GFP, white signal. Scale bar = 2 μ m. **B** C4 synaptic pathology was rescued by simultaneous OE of SNX27 (C4-SNX27-OE). One-way ANOVA. * $p < 0.05$, ** $p < 0.01$. **C** Representative traces of mEPSCs in GFP-control (blue), C4-OE (red), C4-SNX27-OE, (purple), and SNX27-OE (gray) L2/3 mPFC pyramidal neurons from P20–25 animals. Scale bars, 125 ms, 10 pA. **D** mEPSC frequency was decreased in C4-OE relative to GFP-control (Kruskal–Wallis one-way ANOVA. ** $p < 0.01$; GFP-control vs. C4-OE, Dunn's multiple comparison test. *** $p < 0.001$) but was rescued when C4 and SNX27 were co-overexpressed (C4-OE vs. C4-SNX27-OE, Dunn's multiple comparison test. * $p < 0.05$). SNX27-OE alone did not alter mEPSC frequency relative to GFP-control (Con vs. SNX27-OE, Dunn's multiple comparison test. $p > 0.9999$) but was significantly greater than in C4-OE (C4-OE vs. SNX27-OE, Dunn's multiple comparison test. * $p < 0.05$). Hz Hertz. There were no differences in the amplitude (**E**, one-way ANOVA. $p = 0.6241$), Rise 10–90 (**F**, Kruskal–Wallis one-way ANOVA. $p = 0.4346$), and Decay tau (**G**, one-way ANOVA. $p = 0.2122$). $N = 24$ GFP-control cells, from 6 animals. $N = 20$ C4-OE cells, from 4 animals. **B** $N = 8$ control dendrites, $N = 9$ C4-SNX27-OE dendrites, $N = 11$ C4-OE and SNX27-OE dendrites, 3 animals each. **D–G** $N = 25$ C4-SNX27-OE cells, from 4 animals. $N = 22$ SNX27-OE cells, from 5 animals. All graphs, Mean \pm SEM.

we verified prior findings that SNX27 is present in dendritic spines and shafts [31] (Fig. 2C–G). We also observed that C4 and SNX27 colocalized in dendritic spines (Fig. 2C–E, intensity plot and orthogonal view) and shafts (Fig. 2F, G). This suggests that C4 and SNX27 are near each other within the dendrites and dendritic spines and that C4 is associated with the endosomal machinery of neurons. Additionally, we conducted in vivo experiments in mPFC examining L2/3 cortical neuronal expression of C4-GFP via IUE to demonstrate that this immune protein is in dendritic compartments (Fig. 2H, I), where it organizes in intracellular clusters, supporting our STED imaging in vitro data.

Thus, our findings challenge established views on the mechanism of the complement pathway's role in synaptic plasticity by showing that high levels of C4, found in pathological states, reduce synaptic connectivity independent of CR3. This is supported by decreased connectivity seen following overexpression of C4 mutants that lack C3 convertase activity, co-IP of C4 with SNX27, colocalization of C4 and SNX27 in dendrites, and *Snx27* KD phenocopying the C4-OE-induced effects, demonstrating a novel neuronal pathway in which C4 can modify synaptic pathologies.

Increasing neuronal levels of SNX27 rescued the C4 hypoconnectivity phenotype

By interactions through its PDZ domain, SNX27 plays a pivotal role in boosting the recycling of glutamate AMPARs and NMDARs from early endosomes to the plasma membrane [29–31], safeguarding postsynaptic receptors from degradation and promoting synapse formation [33]. To determine whether increased expression of SNX27 in the C4-OE background restored spine deficits, we simultaneously overexpressed C4 and SNX27 (C4-SNX27-OE) (Fig. 3). To ensure that electroporation of three plasmids led to increased expression of all the target genes, we used Multiplex Fluorescence In Situ Hybridization (M-FISH) to quantify the levels of *Gfp*, *C4* and *Snx27* mRNA in electroporated L2/3 cortical cells (Fig. S1A). We confirmed significant overexpression of *Snx27* in GFP-positive cells (Fig. S1B) as well as increased expression of *Snx27* in C4 overexpressing cells (Fig. S1C).

Dendritic spine density in C4-SNX27-OE was indistinguishable from GFP-control, rescuing the C4-induced phenotype (Fig. 3A, B) and suggesting that upregulation of this endosomal protein can counteract C4-OE-driven hypoconnectivity. Notably, overexpression of SNX27 alone (SNX27-OE) did not increase spine density compared to GFP-control (Fig. 3A, B), demonstrating that the SNX27 rescue drives structural spine plasticity through a C4-specific cellular mechanism rather than a general increase in structural synaptic plasticity.

To ascertain the effects of C4-OE and subsequent rescue with SNX27 on spine morphology, we used unbiased k-means clustering on dendritic spine data to classify spines into subtypes (Fig. S2A, B). In our analysis, we found four types of spine clusters. Cluster 1 consists of large mushroom spines with a high head-to-neck ratio, Cluster 2 contains shorter, large-volume stubby spines,

Cluster 3 contains long spines with no head, and Cluster 4 consists of medium-sized spines with a high head-to-neck ratio. We observed that C4-OE resulted in an overall reduction in spine volume across all clusters. Furthermore, Cluster 1 spines showed a significantly reduced head-to-neck ratio with increased levels of C4. (Fig. S2C, D). We also found a decrease in the proportion of Cluster 1 spines, which had the highest head-to-neck ratio, with C4-OE and SNX27 KD, suggesting a common pathological mechanism (Fig. S2E).

C4-SNX27-OE dendrites displayed similar cluster proportions as controls (Fig. S2E), suggesting that increased levels of SNX27 rescue the C4 deficit. Overall, C4-OE led to a smaller spine size, suggesting the weakening of spines as a possible mechanism for spine loss. Endo-lysosome activity and SNX27 activity support the growth and stabilization of dendritic spines during plasticity by regulating membrane growth and the insertion of postsynaptic receptors [29, 34, 35]. Our results indicate that increased levels of C4 may interfere with these intracellular plasticity mechanisms.

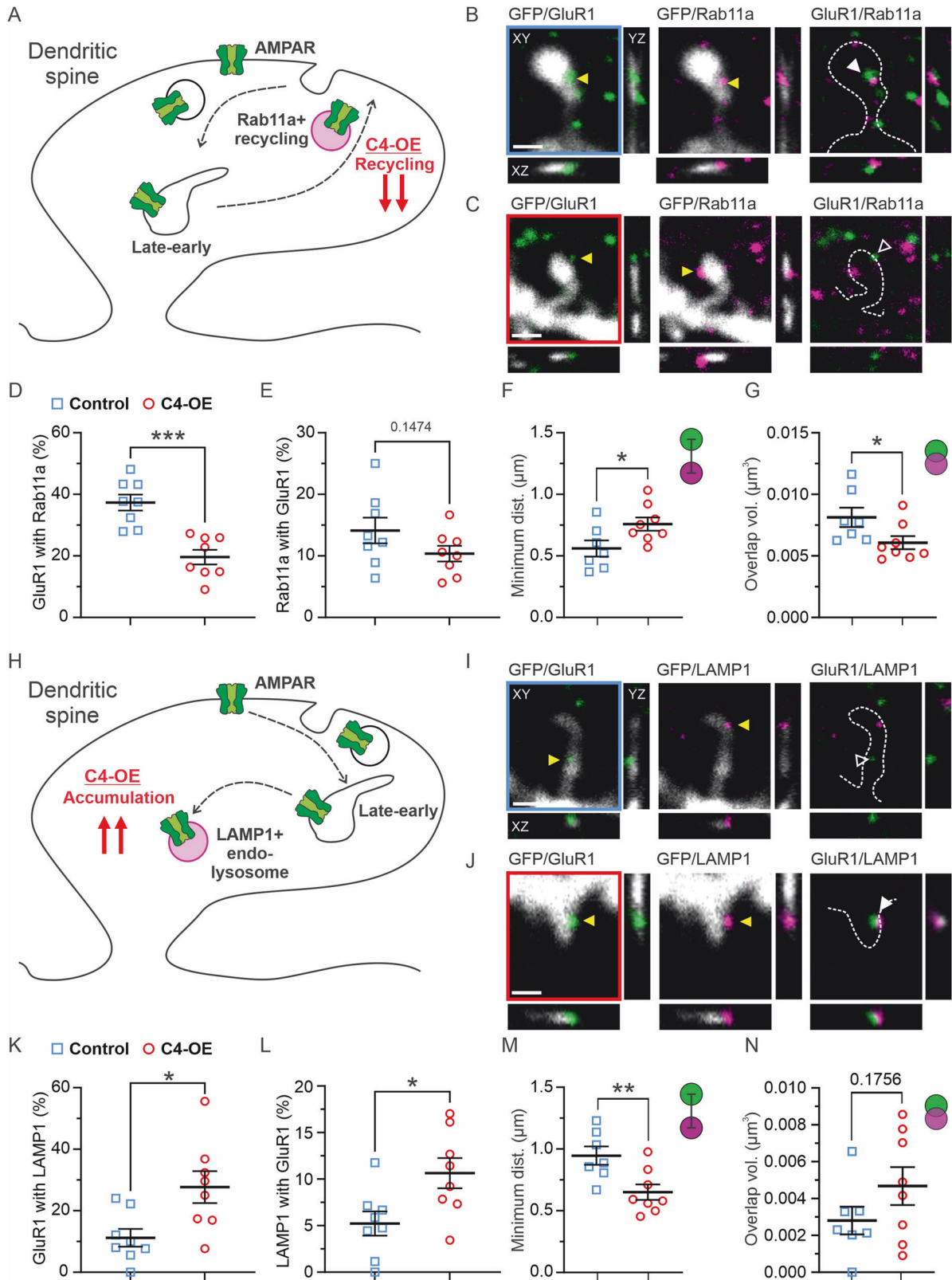
Next, we determined whether the C4-OE-induced morphological alterations and subsequent rescue of these deficits with C4-SNX27-OE (Figs. 1E, S2 and 3A, B) resulted in parallel changes at a functional level (Fig. 3C–G). To test this, we performed electrophysiological whole-cell voltage-clamp recordings in acute brain slices prepared from the mPFC to monitor the excitatory drive of transfected L2/3 neurons. We found that increased levels of C4 led to an approximately 38% reduction in the frequency of miniature excitatory postsynaptic currents (mEPSCs) (Fig. 3C, D) as compared to GFP-control, indicating that C4-OE causes a decrease in functional synaptic connectivity. We also found that C4-SNX27-OE mice did not show this functional deficit, restoring mEPSC frequency to GFP-control levels (Fig. 3D). Importantly, SNX27-OE did not alter mEPSC frequency relative to controls (Fig. 3D), indicating that SNX27 rescues the hypoconnectivity phenotype through a C4-specific mechanism.

In contrast to our previous study [11], we did not identify any significant changes in mEPSC amplitude between groups (Fig. 3E). One reason for the discrepancy might be the different recording solutions used in the two studies and small differences in the developmental windows used for the recordings. Consistent with our previous study, we did not observe any significant differences in mEPSC rise or decay kinetics (Fig. 3F, G, respectively).

These findings indicate that increasing levels of the endosomal protein SNX27 rescues the C4-OE-induced hypoconnectivity phenotype, suggesting a possible link between overexpression of C4, disruption of the synaptic trafficking machinery, and pathological synaptic loss.

C4-OE disrupted GluR1-containing AMPAR trafficking in L1 apical tuft dendritic spines

SNX27 mediates the insertion of AMPAR subunits into the postsynaptic membrane [29], which is necessary to stably increase spine size [32] and promote the effects of experience on synaptic transmission efficacy in vivo [33, 36]. In the past, we demonstrated



that C4-OE impacts the circuitry of the L1 apical tufts [11]. Axonal projections to superficial L1 are part of a circuit that controls consciousness, attention, and learning states [37]. Therefore, we sought to determine whether C4-OE alters the recycling of AMPA GluR1 subunits in the L1 dendritic spine apical tufts of transfected mPFC pyramidal cells.

To do this, we first used immunohistochemistry to stain for GluR1 and the recycling endosome protein Rab11a [38], followed by STED nanoscopy in fixed mPFC tissue sections (Fig. 4A–C). Rab11a triggers the cellular machinery required to sort and recycle membranes and proteins back to the plasma membrane. STED imaging allowed us to inspect the nanoscale organization of the

Fig. 4 C4-OE disrupted GluR1-containing AMPAR trafficking in L1 apical tuft dendritic spines. A Model depicting effects of C4 overexpression on GluR1 recycling in dendritic spines. **B** Representative images (60X) showing a GFP-positive dendritic spine (white), GluR1 (green) and Rab11a (magenta) of P21–23 apical tufts in GFP-controls (blue frame). **C** Representative images (60X) showing a dendritic spine identified with GFP signal (white), GluR1 (green) and Rab11a (magenta) in C4-OE (red frame). **B, C** Yellow arrowhead, GluR1 or Rab11a clusters in spines. White-filled arrowhead, GluR1/Rab11a colocalization. White empty arrowhead, non-colocalized GluR1/Rab11a. Spine silhouette, white dotted line. Orthogonal views are shown (XY, YZ and XZ). Scale bar = 2 μ m. **D** C4-OE caused a 47% decrease in the amount of GluR1 colocalized with Rab11a compared to GFP-control. **E** There was no change in the amount of Rab11a colocalized with GluR1 in C4-OE relative to GFP-control. **F** C4-OE increased the minimum distance between GluR1 and Rab11a clusters by 35% relative to GFP-control. Green circle: GluR1, Magenta circle: Rab11a. **G** C4-OE led to a 25% decrease in the overlapping volume between GluR1 and Rab11a relative to GFP-control. Green circle: GluR1, Magenta circle: Rab11a. **H** Schematic showing the effects of C4-OE on GluR1 degradation in dendritic spines. **I** Representative images (60X) showing a GFP-positive spine (white), GluR1 (green) and LAMP1 (magenta) in GFP-control (blue frame). **J** Representative images (60X) showing a GFP-positive spine (white), GluR1 (green) and LAMP1 (magenta) in C4-OE (red frame). **I, J** Yellow arrowhead, GluR1 or Rab11a clusters in spines. White empty arrowhead, non-colocalized GluR1/LAMP1. White-filled arrowhead, GluR1/LAMP1 colocalization. Spine silhouette, white dotted line. Orthogonal views are shown (XY, YZ and XZ). Scale bar = 2 μ m. **K** C4-OE led to a 145% increase in the amount of GluR1 colocalized with LAMP1. **L** C4-OE caused a 103% increase in the amount of LAMP1 colocalized with GluR1. **M** C4-OE induced a 31% decrease in the minimum distance between GluR1 and LAMP1 clusters. Green circle: GluR1, Magenta circle: LAMP1. **N** Compared to GFP-control, C4-OE did not alter the overlapping volume between GluR1 and LAMP1. Green circle: GluR1, Magenta circle: LAMP1. **D, E, K, L** $N = 8$ dendrites, 3 animals for Con and C4-OE. **F, G, M, N** $N = 7$ dendrites, 3 animals, Con; and $N = 8$ dendrites, 3 animals, C4-OE. **D–G, K–N** t -test. * $p < 0.05$, ** $p < 0.01$, *** $p < 0.001$. All graphs, Mean \pm SEM.

spine by identifying colocalized (Fig. 4B) and non-colocalized (Fig. 4C) GluR1 and Rab11a protein clusters in spine subcompartments. Additionally, we found that C4-OE caused a significant decrease in the quantity of GluR1 clusters colocalizing with Rab11a, while the number of Rab11a-positive clusters associating with GluR1 showed a decreasing trend without reaching significance (Fig. 4D, E). Furthermore, C4-OE in cortical neurons also caused an increase in the minimum distance (Fig. 4F) and a decrease in the degree of overlap (Fig. 4G) of colocalized GluR1-Rab11a clusters, suggesting that C4-OE decreased the association of GluR1 with Rab11a-positive recycling endosome, disrupting the recycling of the receptors to the plasma membrane.

Since we observed that increased levels of C4 resulted in deficits in the recycling of AMPA-containing GluR1 at the spine, we proceeded to determine whether this postsynaptic receptor instead aggregated in the endo-lysosomal compartment. To do this, we looked for GluR1 colocalizing with LAMP1-positive clusters, an endo-lysosomal marker [39, 40] (Fig. 4H–J). LAMP1 is a glycoprotein that is a major component of the endo-lysosomal membrane. We found non-colocalized (Fig. 4I) and colocalized (Fig. 4J) GluR1- and LAMP1-positive clusters in spine compartments. We observed that C4-OE caused increased instances of GluR1 colocalizing with LAMP1 and increased LAMP1 associating with GluR1 (Fig. 4K, L). Additionally, we observed a decrease in the minimum distance between GluR1 and LAMP1 clusters (Fig. 4M), with no significant change in their degree of overlap with increased levels of C4 (Fig. 4N). Compared to GFP-control, increased levels of C4 did not alter the size of GluR1, Rab11a-, and LAMP1-positive clusters in the spine (Fig. S3). These findings demonstrate that elevated levels of neuronal C4 disrupt GluR1 trafficking, favoring postsynaptic receptor accumulation in LAMP1-positive endo-lysosomal compartments, thus contributing to impaired synaptic plasticity.

Since we observed that elevated C4 led to alterations in the localization of GluR1 in recycling and endo-lysosomal compartments, we performed microdissection of transfected mPFC tissue and biochemical experiments (Fig. 5A, Left and Right panels) to determine whether GluR1 protein levels were altered in mPFC tissue. We found that C4-OE increased GluR1 protein levels versus control, with a 2-fold increase in isolated synaptosomes and a 1.2-fold increase in the cytosolic fraction. We utilized the GFP fluorescent signal to precisely delineate the microdissection area containing transfected cells in the mPFC (Fig. 5A, Left panel). Additionally, we found increased levels of GluR1 and the postsynaptic protein PSD95 in synaptosomes compared to the cytosolic fraction to confirm successful synaptosome extraction (Fig. S4A, B). These results suggest that increased levels of C4 led to abnormal accumulation of the postsynaptic receptor in L2/3

cortical neurons. As demonstrated previously, higher levels of C4 did not change the gross somatodendritic morphology or electrical properties of L2/3 mPFC pyramidal cells [11]. Therefore, the synaptic deficits observed with increased levels of C4 are not caused by impacting the health of neurons but rather by disruptions in the trafficking of postsynaptic GluRs.

Lastly, we aimed to determine whether the GluR1 trafficking deficits with C4-OE were linked to changes in translation or protein degradation (Fig. 5B). To do this, we first expressed either GluR1 and SNX27 (**GS**) or GluR1, SNX27, and C4 (**GSC**) in HEK293T cells (Fig. 5B). Next, we blocked translation using cycloheximide (CHX) or both translation and degradation using CHX and MG132 (Fig. 5B). Consistent with previous work [41], we observed that CHX treatment resulted in a reduction of GluR1 expression in GS cells compared to the DMSO condition, which was subsequently restored to DMSO levels following the application of the degradation inhibitor MG132 (Fig. 5C). These experiments also suggest that we can manipulate GluR1 levels in HEK293T cells reliably by pharmacology targeting translation and degradation.

In contrast, in GSC cells, which express C4, we observed no change in GluR1 levels upon CHX treatment (Fig. 5C). Upon initial inspection, it may seem that C4 is interfering with the translation of GluR1. However, consistent with our synaptosome experiments (Fig. 5A), the more probable explanation is that increased levels of C4 led to an abnormal buildup of GluR1 and inhibition of translation for eight hours is not sufficient to reduce levels of the postsynaptic receptor. Subsequent application of CHX + MG132 treatments did not alter GluR1 levels compared to control DMSO or CHX, which suggests that C4 alters the degradation of GluR1. However, because of the function of the endosomal protein SNX27, it is plausible that degradation is still intact but that GluR1s are not being degraded because they are missorted, which is consistent with our super-resolution imaging experiments (Fig. 4).

Taken together, increased levels of the neuroimmune gene C4 led to alterations in GluR1 trafficking, as observed in the mislocalization of the postsynaptic receptor in the recycling and endo-lysosomal compartments and elevated GluR1 protein levels, deficits that are consistent with perturbations of the endo-lysosomal pathway and dysfunction of the sorting nexin retromer complex.

DISCUSSION

We have demonstrated that the decreased connectivity caused by increased expression of C4, a gene associated with SCZ, is not dependent on CR3. This main phagocytic receptor has been postulated to drive complement-mediated synaptic engulfment. Instead, using STED nanoscopy, electrophysiological approaches,

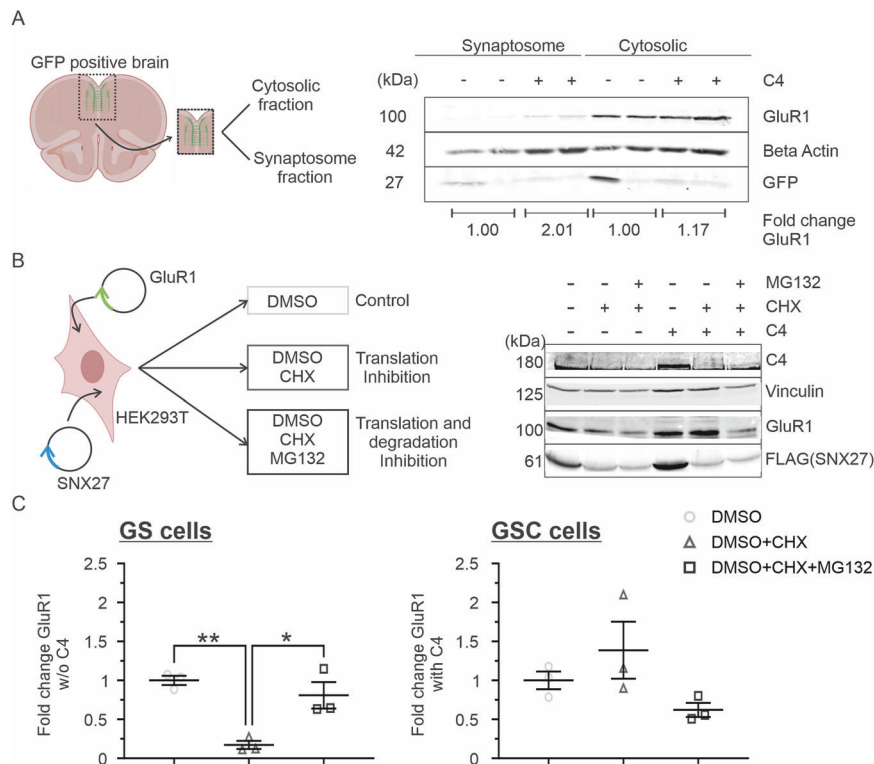


Fig. 5 C4-OE led to increased levels of GluR1-containing AMPAR in mPFC neurons. **A** Left: Schematic of dissected GFP-positive tissue from IUE animals, used for isolating cytosolic and synaptosome fractions. Right: Western blot (WB) showing levels of GluR1 with C4 overexpression. GluR1 levels were detected in synaptosome and cytosolic fractions in control and C4-OE conditions. Since C4 was expressed at relatively low levels, it could only be detected when several brains were pooled. Therefore, each lane corresponds to pooled brain lysate from a single litter (6 mice). Protein molecular weights, kilodaltons (kDa, left column). "+" indicates the presence of C4 (top row). Numbers in the bottom row indicate fold change in GluR1 levels relative to control synaptosome and cytosolic fraction. **B** Left: Schematic of degradation assay in HEK293T cells. Right: WB quantified protein levels of GluR1 in GS and GSC cells with CHX and CHX + MG132 treatment. Protein molecular weights, kilodaltons (kDa, left column). "+" indicates the presence of C4, CHX or MG132. **C** Left: CHX treatment led to decreased GluR1 levels in GS cells, which was rescued upon application of MG132. Right: GluR1 levels in GSC cells were unaffected by CHX or CHX + MG132 treatments. Light gray circles: DMSO treated cells, Dark gray triangles: CHX treated cells, Dark gray squares: CHX + MG132 treated cells. $N = 3$ sample replicates per condition. One-way ANOVA. * $p < 0.05$, ** $p < 0.01$. All graphs, Mean \pm SEM.

and biochemical assays, we demonstrated that C4-OE leads to mislocalization of GluR1 in the recycling and endo-lysosomal compartments and abnormal accumulation of the postsynaptic receptor, which causes the loss of synapses in the mPFC, a region associated with devastating neuropsychiatric disorders [42]. This is further supported by increased levels of SNX27 rescuing the synaptic phenotype in C4 overexpressing cortical neurons. Therefore, we propose a new model where elevated levels of C4 disrupt synaptic plasticity through the dysregulation of GluR1-containing AMPA receptor trafficking and decrease recycling to the postsynaptic membrane. Future research will decipher whether interactions between C4 and SNX27 are direct or occur through a larger protein complex in the postsynaptic spines, as well as whether this interaction is specific to GluR1 or impacts the trafficking of other GluR subunits similarly.

An alternate explanation of the results is that increasing the levels of SNX27 leads to C4 sequestration and limits its availability, which would potentially block microglia-dependent synaptic pruning and inhibit synaptic loss. We believe that this is highly unlikely because we observed C4-induced synaptic loss in the CR3KO background and with overexpression of C4 mutants that lack C3 convertase activity, which will disrupt the complement pathway. In addition, we demonstrated that increased levels of C4 led to the mislocalization of GluR1-containing AMPAR subunits in the recycling and endo-lysosomal compartments and elevated GluR1 protein levels, which is linked to the function of SNX27-retromer complex and established mechanisms of synaptic

plasticity [33, 36, 43] that are not dependent on microglia-mediated synaptic engulfment. SNX27 takes part in receptor recycling through its interaction with different protein complexes via its multiple domains [44]. Previous work has shown that deletion of the PDZ domain of SNX27 led to lowered interaction with GluRs, and reduced recycling as well as increased degradation of GluRs [29]. Lastly, the established mechanism of complement-driven synaptic loss requires enzymatic activity in the extracellular space. However, SNX27 is an intracellular protein that would not interfere with these C4 properties to limit synaptic engulfment. Even if SNX27 sequestered some C4 protein, a small amount of C4 could be sufficient to drive the local pruning of synapses by microglia due to the amplification mechanisms of the complement pathway [4]. However, that is contradictory to our observation, as SNX27 completely rescues the C4 synaptic phenotype when both proteins are overexpressed.

Together with the observation that in HEK293T cells expressing C4, GluR1 levels were not altered by pharmacological inhibition of translation and degradation, our findings demonstrate that C4 might be preventing SNX27 from interacting with the recycling machinery, causing GluR1 to abnormally accumulate in endo-lysosomal compartments, in effect producing a state of GluR1 limbo. In this model, deficits in GluR1 recycling and degradation with increased levels of C4 are a consequence of GluR1 missorting. Further research is needed to determine whether C4 alters trafficking by disrupting specific functional domains in SNX27.

We demonstrated that simultaneous knockdown (KD) of Snx27 and overexpression of C4 did not further reduce spine density compared to the C4-OE condition, and we also showed that SNX27-OE alone could not increase spine density. This suggests a shared downstream pathway for these processes, indicating that increased C4 levels disrupt SNX27 activity rather than these two proteins acting through parallel pathways to control synapse formation. These points together indicate that pathological synaptic loss in the PFC is not directly dependent on canonical complement pathways and, most likely, is associated with disruption of intracellular endo-lysosomal recycling/trafficking signaling.

Overall, both disruptions in the endo-lysosomal pathway and dysfunction of the sorting nexin retromer complex can impair the proper handling and trafficking of proteins within cells [29, 34, 41, 45], leading to protein missorting, aggregation, and the accumulation of toxic protein aggregates, which are hallmark features of several neurodegenerative and lysosomal storage diseases [46–49]. Future research should determine whether endo-lysosomal disruption is specific to neuronal C4 and schizophrenia pathology or whether this is a more general mechanism where pathological levels of other complement proteins, such as C3 and C1q can interact with intracellular proteins in neuron and glia to exacerbate pathological mechanisms. Indeed, increased expression of C1q and C3 is observed in devastating neurodegenerative diseases such as Alzheimer's disease [50, 51] and frontotemporal dementia [52] and mouse models of perioperative neurocognitive disorders [53].

Previous research has shown that complement overactivation leads to the increased accumulation of synaptic material in the microglia lysosome [2, 3, 11, 13, 54, 55], which has been interpreted as enhanced microglia-mediated synaptic phagocytosis. We postulate that microglia could still play a role in synaptic elimination but that they do this by eliminating already weakened synaptic connections or their molecular remnants. In this scenario, microglia-dependent synaptic phagocytosis could be triggered by disrupted synapse formation or an inability to stabilize the synapse. In support of this, our group, as well as others, have demonstrated that C4-OE can result in specific deficiencies in filopodia, the precursors of spine synapses, and a decrease in the proportion of newly acquired dendritic spines [6, 11]. This indicates that rather than accelerating synaptic pruning, increased levels of C4 may contribute to pathological synaptic loss by interfering with the creation and growth of synapses, which are linked to SNX27 function, glutamate receptor recycling, and LTP [43]. Nevertheless, our data suggests that CR3-dependent microglial activity alone cannot fully explain the C4-OE-induced synaptic pathology.

During LTP, SNX27 is translocated to dendritic spines, where it regulates the trafficking of synaptic proteins to the postsynaptic membrane [29, 31]. Additionally, NMDA receptors play a crucial role in LTP, and pharmacological [56, 57] and genetic studies [58] have linked NMDA hypofunction and alterations in specific receptor subunits to SCZ pathophysiology. Although, we did not investigate whether increased levels of C4 led to altered recycling of NMDAR subunits, Druart et al. [6] recently showed that C4-OE leads to NMDAR hypofunction. Additionally, a recent study also demonstrated that SCZ-associated GRIN2A variants are mostly loss-of-function mutations [59], indicating that increased C4 levels lead to a convergent mechanism of SCZ pathophysiology. In support of this, *in vivo* studies have demonstrated that LTP-like plasticity, which is driven, in part, by NMDA activity, is altered in patients with SCZ [60–62].

The neocortex's outermost layer, L1, is highly conserved across species and cortical areas and serves as the primary input layer for top-down information flow [37, 63–66]. Dysregulation of L1 circuitry can disrupt the dynamics of excitation and inhibition, leading to aberrant processing of emotional, cognitive, and social

information observed in SCZ [11, 67]. Using STED nanoscopy, biochemical assays and electrophysiological recordings, we linked altered plasticity in L1 to a specific molecular mechanism, disruptions in the function of the endo-lysosomal pathway and GluR recycling.

Elevated levels of C4 resulted in a decrease in mEPSC frequency without altering their amplitude. This contrasts with the previous findings of Comer et al. [11] and the expected outcomes of interfering with GluR recycling/trafficking on the postsynaptic side. We have consistently observed the C4 phenotype exclusively in the spines of L1 apical tufts. Hence, any variations in the frequency or amplitude of minis detected in the cell body likely originate from these distal sites. Differences in mEPSCs between experimental groups must be robust enough to withstand somatodendritic filtering, influenced by factors such as recording parameters and internal solutions used across studies. Notably, the choice of intracellular solution varies significantly between Comer et al. [11], Phadke, and Druart et al. [6], and this study potentially contributes to observed discrepancies in C4-related findings.

Moreover, age differences in mouse cohorts studied by Comer et al. (P18–P25) versus Phadke and Druart et al. [6] and this study (P20–P30) highlight a critical window for synaptic plasticity during development, a “sweet spot,” where deficits in GluR1 recycling and trafficking causing postsynaptic weakening abruptly led to decreased synaptic density. In fact, Comer et al. noted an 18% reduction in mEPSC amplitude in younger cohorts, possibly reflecting rapid changes in GluR1 trafficking, which could initiate decreases in synaptic density as measured by reduced mEPSC frequency in subsequent studies. Interestingly, Druart et al. [6] reported a reduced rectification index in C4-OE neurons, indicative of an increase in GluA2 subunit-lacking AMPARs, potentially masking a decrease in overall AMPAR number through enhanced Ca²⁺ permeability. This suggests that early deficits in AMPAR trafficking may drive spine loss, with surviving spines possibly maintaining higher densities of GluA2-lacking AMPARs, thereby compensating for reduced AMPAR numbers and influencing synaptic persistence and plasticity mechanisms.

Postnatal development in the mammalian brain is characterized by an early rapid phase of synaptic formation, followed by a slower phase of pruning [68–70]; we propose that in SCZ, early deficits in synapse formation and LTP lead to alterations in the developmental trajectory of synapses, including accelerated synaptic pruning. Our findings support the hypothesis that dysfunction in the glutamatergic system contributes to the development of the disease. Furthermore, they establish a direct link between neuroimmune dysfunction and altered molecular mechanisms of glutamatergic transmission.

Our findings reveal a new mechanism of C4-mediated synapse loss. This discovery is particularly significant in comprehending the wiring of synapses and diseases that stem from complement-driven synaptic pathology. Since treatments that modify the complement pathway or focus on microglia-mediated pathological pruning could have negative impacts on the nervous and immune systems [71], our findings provide a fresh possibility to address the effects of pathological complement activity on the synapse.

MATERIALS AND METHODS

Animals

All experimental protocols were conducted according to the National Institutes of Health (NIH) guidelines for animal research and were approved by the Boston University Institutional Animal Care and Use Committee (IACUC; protocol #2018-539).

All mice were group housed on a 12-h light and dark cycle with the lights on at 7 AM and off at 7 PM and with food and water *ad libitum*.

Offspring were housed with dams until weaning at P21. Experiments were performed in CD-1 wild-type mice of both sexes (CD-1 IGS; Charles River; strain code: 022). P21–23 mice were used for STED and spine density experiments. P20–25 mice were used for electrophysiology experiments. For a subset of spine density experiments, we used P21–23 CR3-KO mice in a C57BL/6 genetic background (The Jackson Laboratory, B6.129S4-Itgamt1Myd/J, Strain #:003991, RRID: IMSR_JAX:00399111) [26].

DNA constructs

For GFP-control, we used a plasmid containing EGFP under the CAG promoter. pCAG-GFP [72] was a gift from Connie Cepko (Addgene plasmid #11150; RRID: Addgene_11150). For C4-OE, DNA sequence containing mouse C4b (NM_009780.2, synthesized by Genescript) was subcloned (InFusion Kit, Clontech) into the pCAG backbone to produce pCAG-C4 [11]. C4-GFP was made by inserting GFP from the pCAG-GFP plasmid C terminus to C4 using a GSSGSS linker (subcloned by Genescript) [11]. For co-electroporation with C4-GFP, mRuby3 under pCAG promoter was used. pCAG-mRuby3-WPRE was a gift from Rylan Larsen (Addgene plasmid #107744; RRID: Addgene_107744). C4-ΔC345C was made by deleting amino acids 1589–1736 using plasmid amplification. For SNX27-OE, we used a plasmid containing SNX27-FLAG under CMV promoter (pCMV-SNX27-FLAG, OriGene Technologies plasmid #MR218832). For SNX27 knockdown experiments, we used plasmids containing scrambled shRNA and anti-SNX27 shRNA under the CMV promoter (pCMV-scr-shRNA, pCMV-shSNX27, Origene Technologies #TL518223). For GluR1 expression in HEK293T cells, we used Gria1 (NM_008165) under the CMV promoter (pCMV6-Gria1, OriGene Technologies plasmid #MC203472). All plasmid DNA was purified using the ZymoPure II (Zymo Research, D4203) plasmid preparation kit and was resuspended in molecular biology-grade water.

HEK293T cell culture

Preparation and maintenance. HEK293T cells were maintained in a 10 cm tissue culture dish (Genesee Scientific, 25-202) in 10 ml of complete media: DMEM (Cytiva, SH30243.01) supplemented with 10% fetal bovine serum (Cytiva, SH30396.03), penicillin (100 units/ml), and streptomycin (100 µg/ml) (Sigma-Aldrich, P4458) following protocols described previously [11]. Cells were kept at 37 °C and 5% CO₂ in a Thermo Scientific HERAccl 150i incubator. Cells were passaged until they reached 90–95% confluency and seeded into a new 10 cm dish at a seeding density of about 2.0 × 10⁶ for maintenance.

Transfection. HEK293T cells were seeded in a 6-well plate (Genesee Scientific, 25-105) at a density of 0.2 × 10⁶ in 2 ml of complete media as described above. Two days after seeding, the cells were transfected using GeneGlide transfection reagent (Biovision, M1081-1000). The complete media in the 6-well plate was replaced by 1 ml per well of DMEM. Two sets of tubes were prepared per transfection condition. Tube 1 contained 500 µl of DMEM along with GeneGlide reagent, and Tube 2 contained 500 µl of DMEM along with plasmid DNA for transfection. One µg of each plasmid was used per well, and 2 µl of GeneGlide per µg of plasmid was used per well. The contents of Tube 2 were mixed with a pipette and transferred gently to Tube 1. After invert mixing the contents, they were incubated at room temperature for 20 min, and drop by drop, they were added to the 6-well plate, followed by gentle swirling. The plate was incubated for 24 h at 37 °C and 5% CO₂, after which the transfection media was replaced by 2 ml of complete media.

Pharmacological inhibition of translation and degradation. HEK293T cells were incubated with either DMSO, 500 µM of Cycloheximide (Sigma-Aldrich, #01810), or 10 µM of MG132 (Sigma-Aldrich, #M8699) for 8 h. After treatment, cell lysates were collected using the protocol described below in “Western Blotting.”

Co-immunoprecipitation and western blotting

Co-immunoprecipitation. HEK293T cells were transfected with three possible conditions: Control with no plasmid, only C4 plasmid, and multiple combinations of two plasmids for testing protein interactions, for example, wt SNX27 and C4 mutant plasmids. 48 h after transfection (as described above), the 6-well plate was removed from the incubator and put on ice. The media in each well was removed, cells were washed with PBS and lysed with 500 µl of lysis buffer consisting of 0.5% NP40 (Boston BioProducts, P-877-250), protease inhibitor cocktail 1X (Thermo Fisher, 87786), 30 mM Tris and 150 mM NaCl, pH 7.5 in Milli-Q water. After

incubation on ice for 15 min, the cells were collected using a cell scraper and transferred to a 1.7 ml microcentrifuge tube. The tube was sealed and rocked with end-over rotation overnight at 4 °C. Following rotation, the tubes were centrifuged at 13,000 rpm for 30 min, and the supernatant was collected for further analysis as a cell lysate. Next, 200 µl of the lysate was incubated with 1:100 dilution of rabbit anti-FLAG antibody (Abcam, ab205606) overnight at 4 °C with end-over rotation. The lysate-antibody mix was then incubated with Magnetic Protein A beads (New England Biolabs, S1425S) overnight at 4 °C with end over rotation. Following incubation with magnetic beads, the beads were separated from the liquid using a neodymium magnet and washed 3 times with 100 µl buffer consisting of 30 mM Tris and 150 mM NaCl in Milli-Q water. Finally, 30 µl of SDS loading buffer (BioRad, 1610747 with 10% 2-Mercaptoethanol) was added to the beads and they were incubated at 95 °C for 5 min to elute protein complexes before using them for Western blots.

Western blotting. HEK293T cell lysate and co-immunoprecipitation elutes were obtained as described above. Samples were size-separated using SDS-PAGE with a 4–20% gradient gel, followed by transfer onto a PVDF membrane (Cytiva, 10600021) for Western blotting analysis. The transfer was carried out at 100 mA constant current, overnight at 4 °C, using a transfer buffer containing 20% methanol, 25 mM Tris pH 7.0 and 100-mM Glycine. Following transfer, the membrane was incubated with a blocking buffer containing 5% nonfat dry milk powder, 0.1% Tween-20, and 0.1% sodium azide in 1X Tris-buffered saline (TBS) (Genesee Scientific, 18-236B), for 1 h at room temperature with tilt shaking. The blocking buffer was removed and replaced with a primary antibody solution (diluted in blocking buffer). The membranes were incubated with primary antibodies overnight at 4 °C with tilt shaking. After incubation, the primary antibody solution was removed and the membranes were washed three times for 10 min each at room temperature with TBST: 0.1% Tween-20, 1X TBS. The membrane was then incubated with a secondary antibody solution (diluted in blocking buffer) overnight at 4 °C with tilt shaking, followed by three washes with TBST. The membrane was then stored in TBST until imaging.

Analysis of western blots. Western blot membranes were imaged using Sapphire Biomolecular Imager (Azure Biosystems, Dublin, CA). Depending on the choice of secondary antibody, either 488 or 640 nm wavelengths were used for the image acquisition. The acquired images were then analyzed in ImageJ using the Gel Analysis Plugin to get intensity values for bands. Each gel run was accompanied by a well containing a protein ladder (Thermo Fisher Scientific, PI26625, Waltham, MA) to help identify the correct molecular weights of bands stained by antibodies. In cases of expression analysis between different conditions, GAPDH (Glyceraldehyde 3-phosphate dehydrogenase) or Vinculin was used as a normalization control.

Antibodies used for western blotting. The following primary antibodies were used for staining: Rabbit anti-C4 (1:300, a gift from Biogen) [11], Mouse anti-GAPDH (1:1000, Santa Cruz Biotechnology, sc-47724), Mouse anti-FLAG (1:1000, Sigma-Aldrich, F3165), Mouse anti-Vinculin (1:1000, Santa Cruz Biotechnology, sc-25336), Rabbit anti-GluR1 (1:300, Millipore Sigma, #04-855). The following secondary antibodies were used for staining: Goat anti-rabbit 647 (1:1000, Sigma-Aldrich, 40839-1ML-F), Goat anti-mouse 488 (1:1000, Jackson ImmunoResearch, 115-545-003), Goat anti-rabbit 488 (1:1000, Jackson ImmunoResearch, 111-545-144).

In utero electroporation

L2/3 progenitor cells in the mPFC were transfected via IUE [11]. Unless otherwise stated, IUE experiments were performed in two- to three-month-old CD-1 dams. All plasmids were used at a final concentration of 1 µg/µl. To generate GFP-control, we electroporated with the pCAG-GFP plasmid. To generate C4-OE, we co-electroporated the pCAG-GFP and pCAG-C4 plasmids. To overexpress C4 mutants, we co-electroporated the pCAG-GFP with pCAG-C4-ΔC345C plasmid to generate C4-ΔC345C-OE and we electroporated pCAG-mRuby3 with pCAG-C4-GFP plasmid to generate C4-GFP-OE.

To generate SNX27-OE, we co-electroporated the pCAG-GFP with the pCMV-SNX27-FLAG; and to generate C4-SNX27-OE, we co-electroporated the pCAG-GFP, pCAG-C4 and pCMV-SNX27-FLAG. For SNX27 knockdown experiments, pCAG-EGFP was co-electroporated with the pCMV-scr-shRNA or pCMV-shSNX27 for scr-shRNA and shSNX27 groups, respectively. For experiments using the CR3KO mice, we electroporated the pCAG-GFP

plasmid in the CR3KO mouse to generate CR3KO-control and co-electroporated the pCAG-EGFP and pCAG-C4 plasmid to generate CR3KO-C4-OE.

Prior to surgery, all tools were sterilized by autoclaving. Aseptic techniques were maintained throughout the procedure, and a sterile field was prepared before surgery using sterile cloth drapes. Animals were weighed, and a combination of buprenorphine (3.25 mg/kg; SC, Bimeda, Inc) and meloxicam (1–5 mg/kg; SC, Covetrus North America) was administered as a preoperative analgesic. Timed-pregnant female CD-1 or CR3KO mice at E16 were anesthetized by inhalation of 4% isoflurane (Covetrus North America) and maintained with 1–1.5% isoflurane via mask inhalation. The abdomen was sterilized with 10% povidone-iodine and 70% isopropyl alcohol (repeated 3 times) before a vertical incision was made in the skin and then in the abdominal wall. The uterine horn was then exposed to allow injection of 0.5–1.0 μ l of DNA solution (containing 1 μ g/ μ l plasmid and 0.1% Fast Green) into the lateral ventricles using a pressure-injector (Picospritzer III, Parker Hannifin) with pulled-glass pipettes (Sutter Instrument, BF150-117-10).

To target L2/3 progenitor cells in PFC for imaging and electrophysiological experiments, a custom-built triple electrode probe was placed by the head of the embryo, with the negative electrodes placed near the lateral ventricles and the positive electrode placed just rostral of the developing PFC [11, 73, 74]. Next, four-square pulses (pulse duration: 50 ms, pulse amplitude: 36 V, interpulse interval: 500 ms) were delivered to the head of the embryo using a custom-built electroporator. Embryos were regularly moistened with warmed sterile PBS during the surgical procedure. After electroporation, the embryos and uterine horn were gently placed back in the dam's abdominal cavity and the muscle and skin were sutured (using absorbable and nonabsorbable sutures, respectively). Finally, the dams were allowed to recover in a warm chamber for 1 h and then returned to their cage.

Primary neuronal cultures

Cortical primary neurons were isolated and cultured according to Beaudoin et al. [75], with minor adjustments. Briefly, E18 pregnant CD-1 dams were deeply anesthetized with an overdose of isoflurane, and an abdominal incision was made to access the uterine horn. Embryos were removed and moved to ice-cold dissociation media as described in Beaudoin et al. [75]. After extraction from the skull, the mPFC was dissected from each hemisphere and collected in fresh dissociation media. After dissection, the tissue was washed and digested with trypsin (Worthington, #LS003707) solution for 20 min at 37 °C, and then Benzoyl-L-histidine-L-lysine (Sigma-Aldrich, #E1014-5KU) was added for an additional 5 min. Digested tissue was washed gently twice with dissection media, then twice with plating media, before being resuspended in plating media and gently triturated with 10 and 1 ml pipettes. Cells were plated on poly-L-lysine coated coverslips at a density of 250,000 cells, and the media was aspirated and changed to maintenance media after allowing the cells to adhere for 6 h. After 48 h, cytosine arabinoside (araC, Sigma-Aldrich C1768) was added to a final concentration of 4 μ M to inhibit non-neuronal cell growth, and then media was changed again after another 24 h to maintenance media without araC. Neurons were grown for 14 days before fixation with 4% paraformaldehyde + 4% glucose before antibody staining.

STED super-resolution microscopy

Perfusions and immunohistochemistry. Mice were administered an overdose of sodium pentobarbital (250 mg/kg, Patterson Veterinary, 07-894-1075) intraperitoneally before transcardial perfusion with phosphate buffered saline (PBS, Gibco, Life Science Technologies, 70011044) then 4% paraformaldehyde (PFA) in PBS. The brains were extracted and postfixed in 4% PFA for 24 h, then transferred to a 30% (w/v) sucrose solution and stored at 4 °C. The tissue was sectioned at 40 μ m thickness with a freezing stage sliding microtome (Leica Biosystems, SM2000). To prepare for immunostaining, the slices were blocked and permeabilized in a blocking buffer: 10% donkey serum (Sigma-Aldrich, S30-100ML) + 1% TritonX100 (Sigma-Aldrich, X100-100ML) in PBS. Next, the brain slices were incubated with primary antibodies on a shaker at 4 °C for 48 h and then with secondary antibodies in the same fashion. After primary incubation, slices were rinsed with 0.025% TritonX100 in PBS for 15 min, four times. After secondary incubation, slices were rinsed with PBS for 15 min, four times. The brain slices were mounted onto 1 mm microscope slides (Corning, Cat # 2975-225) with DAPI-free mounting media (Thermo Fisher Scientific, p36965).

Depending on the experiment, the following primary antibodies were used: Rabbit anti-C4 (1:500, Biogen) [11], Mouse anti-FLAG (1:1000, Sigma-

Aldrich, F3165), Mouse anti-GluR1 (1:250, NBP2-22399, Novus Biologicals), Rabbit anti-Rab11a (1:250, Fisher Scientific, 71-5300), Rabbit anti-LAMP1 (1:500, abcam, ab24170). The following secondary antibodies were used: anti-Mouse Abberior STAR Orange (1:300, Fisher Scientific, NC1933863), and anti-Rabbit Abberior STAR Red (1:1000, Fisher Scientific, NC1933870).

Imaging. Fluorescence data was acquired using an inverted laser scanning confocal microscope (Nikon Instruments, Nikon Ti2 with Perfect Focus, Plan apochromat 60 \times 1.4 NA oil immersion objective, Physik Instrumente P736 Piezo Z-stage) outfitted with an Abberior Facility Line STED system controlled with the Abberior Inspector software platform. The 485 nm (for GFP-cell fill), 561 nm (Abberior STAR Orange), and 640 nm (Abberior STAR Red) pulsed excitation lasers and a 775 nm STED depletion laser (Abberior STAR Orange Abberior STAR Red) were used to obtain 25 nm pixel size. For dendrite, synaptic marker, and endosomal marker imaging, ROIs localized to apical dendritic tufts in L1 were acquired consisting of stacks of images (first 50 μ m below the pia, approximately 20–40 optical sections, Z-step = 0.2 μ m) and saved in OBF file format.

Image processing and deconvolution. OBF image files were converted to 32-bit TIFF format and combined to make a single 3-channel image in ImageJ, then imported to IMARIS and converted to IMS file format. To compensate for the difference in resolving power on the Z axis, Z-axial distances were adjusted from 0.2 to 0.1 μ m before deconvolution [76]. Using the IMARIS image processing module, the channels for synaptic and endosomal markers (Abberior STAR Orange, Abberior STAR Red) were deconvolved with 10 iterations of the Robust (iterative) algorithm, with Z axial denoising of filter size 0.7.

IMARIS reconstruction. Dendrites were digitally reconstructed in IMARIS using the software's semi-automatic filament reconstruction function, based on the GFP signal. Dendrite shafts were aligned using seedpoints, and spines were reconstructed by hand using the create function and auto-align feature. The Approximate Circle of Cross Section Area algorithm was used to calculate both the dendrite and spine diameters. To increase the confidence in puncta reconstruction for analysis, each punctate signal was reconstructed as spots and surfaces. Spots and surfaces were used to describe protein clusters and the morphology of dendritic spines and were filtered according to custom parameters, those verified with a cluster size distribution analysis of each protein (i.e., GluR1, Rab11a, LAMP1). Cluster sizes were determined by setting visual thresholds for each stain individually for 5 images, followed by fitting a Gaussian curve to the obtained distribution to calculate mean puncta sizes. Spots were determined to be inside the dendrite (dendritic spots) using the Spots Close to Filament Border IMARIS extension, with distances for each protein signal determined based on the cluster size distribution analysis (0.18 μ m for GluR1, Rab11a and LAMP1). Surfaces were manually filtered according to the dendritic spots (dendritic surfaces).

IMARIS analysis

Dendrite: After dendrites were digitally reconstructed, dendrite information was exported as CSV files containing values for the dendrite area, position, volume, spine length, spine area, spine volume, and spine position. Characterization of dendritic surfaces: Dendritic surfaces, as described in the reconstruction section, were first exported as a batch. Following this, the same surfaces were manually assigned as spine head or neck-associated puncta (protein clusters), and their parameters were exported on a per-spine basis. Each surface export resulted in CSV files containing values for the surface area, volume, intensity, position, and percentage of overlap with neighboring surfaces.

Colocalization of dendritic spots: Dendritic spots were determined to be colocalized using the IMARIS colocalize spots extension, using 0.25 μ m based on the cluster size distribution analysis.

Dendritic spine confocal analysis

Spine density. To determine dendritic spine density, images were acquired using an inverted laser scanning confocal microscope (Nikon Instruments, Nikon Eclipse Ti with C2Si+ confocal) controlled via NisElements (Nikon Instruments, version 4.51) using a 488 nm laser. Images were taken with a 60 \times Plan Apo objective (Nikon Instruments; Plan Apo, NA 1.4, oil immersion objective) and Z-stack images were acquired using a step size of 0.2 μ m. The brightest dendrites were selected from each image to ensure that the dim protrusions, such as filopodia, were

reliably identified. To reliably identify the spines of a given dendrite, we analyzed GFP-positive dendrites that were not occluded by other nearby cell processes. Dendrite selection and all following spine analyses were conducted blindly. Dendritic spine density was calculated using the Filament reconstruction function in IMARIS. Each target dendrite was first manually traced using the filament tool. The center of the trace was set to automatic to allow the software to best estimate the shape of the dendrite. Each dendritic filament was approximately 50–70 μm in length. Only unbranched, single stretches of dendrites ending in tufts were used for spine density analysis. Following dendrite tracing using the filament tool, the IMARIS slice view function was used to estimate the thinnest spine heads as well as the largest spine lengths (0.15 and 3.10 μm , respectively). These numbers were then used to reconstruct spines, allowing for branching (this refers to branched spines being allowed as a reconstruction, and counted as separate spines). Next, each spine was manually assessed for accuracy using the position of spine terminal points and spines were either deleted or drawn in as necessary. Once we obtained the number of spines per dendritic branch, we divided this number by the total dendritic branch length (>50 μm) to obtain spine density values. IMARIS-generated morphological parameters were exported to CSV files for further analysis.

Morphology analysis. IMARIS-generated spine parameters were used to divide dendritic spines into 4 clusters using the k-means algorithm, which were determined using silhouette analysis. Clusters were defined on control spines, using Spine Length, Spine Volume, Spine Head Volume, Spine Neck Volume, Spine Head Width, Spine Neck Width, and Head to Neck Ratio. Once clusters were defined, each spine of the other conditions was assigned to one of the 4 clusters based on their distance to each of the cluster centroids.

Electrophysiological recordings and analysis

Mice (P20–25) were anesthetized with a 4% isoflurane-oxygen mixture (v/v) and perfused intracardially with an ice-cold Perfusion/Slicing artificial cerebrospinal fluid (P/S aCSF) bubbled with 95% O₂/5% CO₂ containing the following (in mM): 3 KCl, 26 NaHCO₃, 1.25 NaH₂PO₄, 212 sucrose, 10 glucose, 0.2 CaCl₂, and 7 MgCl₂ (300–310 mOsm). Coronal slices (300 μm thickness) were cut in the same P/S aCSF using a VT1000 S (Leica, Wetzlar, Germany) vibratome before being transferred to a Recording aCSF solution bubbled with 95% O₂/5% CO₂ containing the following (in mM): 125 NaCl, 2.5 KCl, 25 NaHCO₃, 1.4 NaH₂PO₄, 16 glucose, 0.4 Na-ascorbate, 2 N-ppyrivate, 2 CaCl₂, and 1 MgCl₂ (300–310 mOsm). Slices were incubated in this Recording aCSF for 30 min at 35 °C before being allowed to recover at room temperature for 1 h prior to recording. All recordings were performed at 29–31 °C. Only electroporated neurons in L2/3 of the prelimbic, infralimbic, and anterior cingulate cortex divisions of the mPFC were recorded from. Signals were recorded with a 5X gain, low-pass filtered at 6 kHz, and digitized at 10 kHz using a patch-clamp amplifier (Multiclamp 700B, Molecular Devices, San Jose, CA).

Whole-cell voltage-clamp recordings were made using 3–5 M Ω borosilicate pipettes filled with an internal solution that contained the following (in mM): 120 Cs-methane sulfonate, 8 NaCl, 10 HEPES, 10 CsCl, 10 Na₂-phosphocreatine, 3 QX-314-Cl, 2 Mg²⁺ + -ATP, 0.2 EGTA (293 mOsm, adjusted to pH 7.3 with CsOH). Series resistance (R_s) and input resistance (R_{in}) were monitored throughout the experiment by measuring the capacitive transient and steady-state deflection in response to a –5 mV test pulse, respectively. For mEPSCs recordings, cells were voltage clamped at –70 mV in the presence of tetrodotoxin (TTX, 1 μM , HelloBio) and picrotoxin (PTX, 100 μM , HelloBio). Liquid junction potentials were left uncompensated. mEPSCs were identified and their amplitude, frequency, rise, and decay were determined using custom scripts written in MATLAB (MathWorks, Natick, MA). At least 120 s were analyzed for each cell. Cells were excluded if R_s varied by more than 5 M Ω or exceeded 20 M Ω at any point during the recordings. For each condition, 20–25 cells were recorded from a total of 4–6 animals across 2–3 litters. All electrophysiology reagents were purchased from Sigma-Aldrich (St. Louis, MO) unless otherwise stated.

Synaptosome extraction

Synaptosomes were extracted using the Syn-PER Kit (Thermo 87793). Briefly, mice were euthanized via isoflurane overdose, and using fluorescent signal under a microscope (10X objective) the mPFC was micro-dissected from both hemispheres and placed into Syn-PER reagent in an Eppendorf tube, pooling tissue from littermates (due to low levels of

protein). Tissue was then homogenized via a dounce and transferred to new tubes for centrifugation at 1200 $\times g$ for 10 min at 4 °C. The supernatant was then collected and re-centrifuged at 15,000 $\times g$ for 20 min at 4 °C. From this, the supernatant was collected as the cytosolic fraction, and the pellet was resuspended in Syn-PER reagent as the synaptosome fraction. These fractions were then used as the lysates for Western blots.

Multiplex fluorescent in situ hybridization

Mice were euthanized via isoflurane overdose, and whole brains were extracted, embedded in OCT, and flash-frozen on dry ice. Brains were stored at –80 °C until slicing. Using a cryostat, tissue sections were sliced 18 μm thick and mounted on Superfrost Plus slides (Fisher 12-550-15). Tissue sections were stained using the RNAScope Multiplex V2 kit (ACDBio 323100) with the ancillary kit for 750 nm dyes (ACDBio 323120), with probes for GFP, mC4, Rbfox3, and SNX27. In addition, sections were stained with DAPI for nuclei identification. Stained sections were imaged using a Nikon spinning disk confocal microscope with a 40X water immersion objective (NA 1.15) with a z step of 0.3 μm . Images were acquired from 5 different XY coordinates across 2–3 tissue sections per animal.

For expression analysis, images were max projected and used as input for CellProfiler (Stirling 2021). In CellProfiler, cells were segmented based on the DAPI signal, and the mean intensity of each channel was measured per cell. Cells were also classified by mean intensity into GFP positive/negative cells, or C4 positive/negative cells using the average value of mean intensity of C4 across all cells as a threshold. For each of the categories of cells, SNX27 expression was calculated using the mean intensity of the signal. Fold change was determined by normalizing to either SNX27 expression in GFP-negative cells or SNX27 expression in C4-negative cells.

Statistical analysis

For confocal and STED image analysis and electrophysiological recordings, we focused on L2/3 neurons in the anterior cingulate cortex, prelimbic, infralimbic, and medial orbital divisions of the mPFC [11]. All statistical analysis was completed in GraphPad Prism 8.0 (GraphPad Software, San Diego, CA) and the threshold for significance for all tests was set to 0.05 ($\alpha = 0.05$). Spine density, electrophysiological data and Western blot expression data were analyzed using a one-way ANOVA followed by Tukey's posttest or a Student's *t* test. Spine morphology was analyzed by using either a Chi-square test or a Student's *t* test. Both male and female mice were used, and we have previously shown that increased levels of C4 in L2/3 mPFC pyramidal cells do not cause sex-dependent differences in connectivity or PFC-associated behavior in mice [11]. Analysis was performed blind to condition. Figures were prepared using CorelDRAW Graphics Suite X8 (Corel Corporation, Alludo, Ottawa, Canada) and ImageJ (NIH, Bethesda, MD). Data are presented as the Mean \pm SEM, unless otherwise noted.

DATA AVAILABILITY

Data are available at https://osf.io/6fvc2/?view_only=7244902b28c840608cd4b0532645ba80.

CODE AVAILABILITY

Custom-written routines are available at https://github.com/CruzMartinLab/IMARIS_compiler and https://github.com/CruzMartinLab/Ephys_analysis_code.

REFERENCES

- Schafer DP, Lehrman EK, Kautzman AG, Koyama R, Mardinly AR, Yamasaki R, et al. Microglia sculpt postnatal neural circuits in an activity and complement-dependent manner. *Neuron*. 2012;74:691–705.
- Schafer DP, Stevens B. Phagocytic glial cells: sculpting synaptic circuits in the developing nervous system. *Curr Opin Neurobiol*. 2013;23:1034–40.
- Stevens B, Allen NJ, Vazquez LE, Howell GR, Christopherson KS, Nouri N, et al. The classical complement cascade mediates CNS synapse elimination. *Cell*. 2007;131:1164–78.
- Dunkelberger JR, Song W-C. Complement and its role in innate and adaptive immune responses. *Cell Res*. 2010;20:34–50.
- Sekar A, Bialas AR, De Rivera H, Davis A, Hammond TR, Kamitaki N, et al. Schizophrenia risk from complex variation of complement component 4. *Nature*. 2016;530:177–83.

6. Druart M, Nosten-Bertrand M, Poll S, Crux S, Nebeling F, Delhaye C, et al. Elevated expression of complement C4 in the mouse prefrontal cortex causes schizophrenia-associated phenotypes. *Mol Psychiatry*. 2021;1–13. <https://doi.org/10.1038/s41380-021-01081-6>.
7. Cao W, Zheng D, Wang G, Zhang J, Ge S, Singh M, et al. Modelling biological age based on plasma peptides in Han Chinese adults. *Aging*. 2020;12:10676–86.
8. Carpanini SM, Torvell M, Morgan BP. Therapeutic inhibition of the complement system in diseases of the central nervous system. *Front Immunol*. 2019;10:362.
9. Reus LM, Pasaniuc B, Posthuma D, Boltz T, Ferrari R, Hernandez DG, et al. Gene expression imputation across multiple tissue types provides insight into the genetic architecture of frontotemporal dementia and its clinical subtypes. *Biol Psychiatry*. 2021;89:825–35.
10. Zinellu A, Mangoni AA. Serum complement C3 and C4 and COVID-19 severity and mortality: a systematic review and meta-analysis with meta-regression. *Front Immunol*. 2021;12:696085.
11. Comer AL, Jinadasa T, Sriram B, Phadke RA, Kretsge LN, Nguyen TPH, et al. Increased expression of schizophrenia-associated gene C4 leads to hypoconnectivity of prefrontal cortex and reduced social interaction. *PLoS Biol*. 2020;18:e3000604.
12. Yilmaz M, Yalcin E, Presumej J, Aw E, Ma M, Whelan CW, et al. Overexpression of schizophrenia susceptibility factor human complement C4A promotes excessive synaptic loss and behavioral changes in mice. *Nat Neurosci*. 2021;24:214–24.
13. Stephan AH, Barres BA, Stevens B. The complement system: an unexpected role in synaptic pruning during development and disease. *Annu Rev Neurosci*. 2012;35:369–89.
14. Mao Y-T, Zhu JX, Hanamura K, Iurilli G, Datta SR, Dalva MB. Filopodia conduct target selection in cortical neurons using differences in signal kinetics of a single kinase. *Neuron*. 2018;98:767–82.e8.
15. Cruz-Martín A, Crespo M, Portera-Cailliau C. Delayed stabilization of dendritic spines in fragile X mice. *J Neurosci*. 2010;30:7793–803.
16. Lüscher C, Nicoll RA, Malenka RC, Muller D. Synaptic plasticity and dynamic modulation of the postsynaptic membrane. *Nat Neurosci*. 2000;3:545–50.
17. Kulik YD, Watson DJ, Cao G, Kuwajima M, Harris KM. Structural plasticity of dendritic secretory compartments during LTP-induced synaptogenesis. *eLife*. 2019;8:e46356.
18. Harris KM. Structure, development, and plasticity of dendritic spines. *Curr Opin Neurobiol*. 1999;9:343–8.
19. Segal M. Dendritic spines and long-term plasticity. *Nat Rev Neurosci*. 2005;6:277–84.
20. Gasque P, Fontaine M, Morgan BP. Complement expression in human brain. Biosynthesis of terminal pathway components and regulators in human glial cells and cell lines. *J Immunol*. 1995;154:4726–33.
21. Chen Y, Chu JMT, Chang RCC, Wong GTC. The complement system in the central nervous system: from neurodevelopment to neurodegeneration. *Biomolecules*. 2022;12:337.
22. Veerhuis R, Janssen I, De Groot CJA, Van Muiswinkel FL, Hack CE, Eikelenboom P. Cytokines associated with amyloid plaques in Alzheimer's disease brain stimulate human glial and neuronal cell cultures to secrete early complement proteins, but not C1-inhibitor. *Exp Neurol*. 1999;160:289–99.
23. Veerhuis R, Nielsen HM, Tenner AJ. Complement in the brain. *Mol Immunol*. 2011;48:1592–603.
24. West EE, Kemper C. Complosome—the intracellular complement system. *Nat Rev Nephrol*. 2023;19:426–39.
25. Kiousis D, Pachnis V. Immune and nervous systems: more than just a superficial similarity? *Immunity*. 2009;31:705–10.
26. Coxon A, Rieu P, Barkalow FJ, Askari S, Sharpe AH, von Andrian UH, et al. A novel role for the $\beta 2$ integrin CD11b/CD18 in neutrophil apoptosis: a homeostatic mechanism in inflammation. *Immunity*. 1996;5:653–66.
27. Kidmose RT, Laursen NS, Dobó J, Kjaer TR, Sirotkina S, Yatime L, et al. Structural basis for activation of the complement system by component C4 cleavage. *Proc Natl Acad Sci USA*. 2012;109:15425–30.
28. Huttlin EL, Bruckner RJ, Paulo JA, Cannon JR, Ting L, Baltier K, et al. Architecture of the human interactome defines protein communities and disease networks. *Nature*. 2017;545:505–9.
29. Hussain NK, Diering GH, Sole J, Anggono V, Huganir RL. Sorting Nexin 27 regulates basal and activity-dependent trafficking of AMPARs. *Proc Natl Acad Sci USA*. 2014;111:11840–5.
30. Lauffer BEL, Melero C, Temkin P, Lei C, Hong W, Kortemme T, et al. SNX27 mediates PDZ-directed sorting from endosomes to the plasma membrane. *J Cell Biol*. 2010;190:565–74.
31. Loo LS, Tang N, Al-Haddawi M, Stewart Dawe G, Hong W. A role for sorting nexin 27 in AMPA receptor trafficking. *Nat Commun*. 2014;5:3176.
32. Hill TC, Zito K. LTP-induced long-term stabilization of individual nascent dendritic spines. *J Neurosci*. 2013;33:678–86.
33. Huo Y, Gao Y, Zheng Q, Zhao D, Guo T, Zhang S, et al. Overexpression of human SNX27 enhances learning and memory through modulating synaptic plasticity in mice. *Front Cell Dev Biol*. 2020;8:595357.
34. Park M, Salgado JM, Ostroff L, Helton TD, Robinson CG, Harris KM, et al. Plasticity-induced growth of dendritic spines by exocytic trafficking from recycling endosomes. *Neuron*. 2006;52:817–30.
35. Nishino H, Saito T, Wei R, Takano T, Tsutsumi K, Taniguchi M, et al. Research articles, cellular/molecular The LMTK1-TBC1D9B-Rab11A cascade regulates dendritic spine formation via endosome trafficking. *J Neurosci*. 2019;39:9491–502.
36. Takahashi T, Svoboda K, Malinow R. Experience strengthening transmission by driving AMPA receptors into synapses. *Science*. 2003;299:1585–8.
37. Schuman B, Dellal S, Prönneke A, Machold R, Rudy B. Neocortical layer 1: an elegant solution to top-down and bottom-up integration. *Annu Rev Neurosci*. 2021;44:221–52.
38. Esteves da Silva M, Adrian M, Schätzle P, Lipka J, Watanabe T, Cho S, et al. Positioning of AMPA receptor-containing endosomes regulates synapse architecture. *Cell Rep*. 2015;13:933–43.
39. Goo MS, Sancho L, Slepak N, Boassa D, Deerinck TJ, Ellisman MH, et al. Activity-dependent trafficking of lysosomes in dendrites and dendritic spines. *J Cell Biol*. 2017;216:2499–513.
40. Cheng X-T, Xie Y-X, Zhou B, Huang N, Farfel-Becker T, Sheng Z-H. Characterization of LAMP1-labeled nondegradative lysosomal and endocytic compartments in neurons. *J Cell Biol*. 2018;217:3127–39.
41. Wang X, Zhao Y, Zhang X, Badie H, Zhou Y, Mu Y, et al. Loss of sorting nexin 27 contributes to excitatory synaptic dysfunction via modulation of glutamate receptor recycling in Down syndrome. *Nat Med*. 2013;19:473–80.
42. Chini M, Hanganu-Opatz IL. Prefrontal cortex development in health and disease: lessons from rodents and humans. *Trends Neurosci*. 2021;44:227–40.
43. Kopec CD, Li B, Wei W, Boehm J, Malinow R. Glutamate receptor exocytosis and spine enlargement during chemically induced long-term potentiation. *J Neurosci*. 2006;26:2000–9.
44. Chandra M, Kendall AK, Jackson LP. Toward understanding the molecular role of SNX27/retromer in human health and disease. *Front Cell Dev Biol*. 2021;9:642378.
45. Pensalfini A, Kim S, Subbanna S, Bleiwas C, Goulbourne CN, Stavrides PH, et al. Endosomal dysfunction induced by directly overactivating Rab5 recapitulates prodromal and neurodegenerative features of Alzheimer's disease. *Cell Rep*. 2020;33:108420.
46. Ross CA, Poirier MA. Protein aggregation and neurodegenerative disease. *Nat Med*. 2004;10:S10–17.
47. Cox TM, Cachón-González MB. The cellular pathology of lysosomal diseases. *J Pathol*. 2012;226:241–54.
48. Zaharija B, Bradshaw NJ. Aggregation of disrupted in schizophrenia 1 arises from a central region of the protein. *Prog Neuropsychopharmacol Biol Psychiatry*. 2024;130:110923.
49. Zempel H, Mandelkow E. Lost after translation: misrouting of Tau protein and consequences for Alzheimer disease. *Trends Neurosci*. 2014;37:721–32.
50. Dejanovic B, Wu T, Tsai M-C, Graykowski D, Gandham VD, Rose CM, et al. Complement C1q-dependent excitatory and inhibitory synapse elimination by astrocytes and microglia in Alzheimer's disease mouse models. *Nat Aging*. 2022;2:837–50.
51. Chatterjee M, Özdemir S, Kunadt M, Koel-Simmelnik M, Boiten W, Piepkorn L, et al. C1q is increased in cerebrospinal fluid-derived extracellular vesicles in Alzheimer's disease: a multi-cohort proteomics and immuno-assay validation study. *Alzheimers Dement*. 2023;19:4828–40.
52. van der Ende EL, Heller C, Sogorb-Esteve A, Swift IJ, McFall D, Peakman G, et al. Elevated CSF and plasma complement proteins in genetic frontotemporal dementia: results from the GENFI study. *J Neuroinflammation*. 2022;19:217.
53. Xiong C, Liu J, Lin D, Zhang J, Terrando N, Wu A. Complement activation contributes to perioperative neurocognitive disorders in mice. *J Neuroinflammation*. 2018;15:254.
54. Bohlson SS, Tenner AJ. Complement in the brain: contributions to neuroprotection, neuronal plasticity, and neuroinflammation. *Annu Rev Immunol*. 2023;41:431–52.
55. Badimon A, Strasburger HJ, Ayata P, Chen X, Nair A, Ikegami A, et al. Negative feedback control of neuronal activity by microglia. *Nature*. 2020;586:417–23.
56. Nakazawa K, Sapkota K. The origin of NMDA receptor hypofunction in schizophrenia. *Pharmacol Ther*. 2020;205:107426.
57. Coyle JT, Tsai G, Goff D. Converging evidence of NMDA receptor hypofunction in the pathophysiology of schizophrenia. *Ann N Y Acad Sci*. 2003;1003:318–27.
58. Singh T, Poterba T, Curtis D, Akil H, Al Eissa M, Barchas JD, et al. Rare coding variants in ten genes confer substantial risk for schizophrenia. *Nature*. 2022;604:509–16.
59. Shepard N, Baez-Nieto D, Iqbal S, Campbell AJ, Pan JQ, Sheng M, et al. Functional analysis of human GRIN2A mutations associated with schizophrenia and

- neurodevelopmental disorders reveals distinct pathological mechanism. [Preprint] 2023. Available from: <https://doi.org/10.1101/2023.08.02.551645>.
60. Hasan A, Nitsche MA, Rein B, Schneider-Axmann T, Guse B, Gruber O, et al. Dysfunctional long-term potentiation-like plasticity in schizophrenia revealed by transcranial direct current stimulation. *Behav Brain Res.* 2011;224:15–22.
 61. Frantseva MV, Fitzgerald PB, Chen R, Möller B, Daigle M, Daskalakis ZJ. Evidence for impaired long-term potentiation in schizophrenia and its relationship to motor skill learning. *Cereb Cortex.* 2008;18:990–6.
 62. Valstad M, Roelfs D, Slapø NB, Timpe CMF, Rai A, Matziorinis AM, et al. Evidence for reduced long-term potentiation-like visual cortical plasticity in schizophrenia and bipolar disorder. *Schizophr Bull.* 2021;47:1751–60.
 63. D'Souza RD, Burkhalter A. A laminar organization for selective cortico-cortical communication. *Front Neuroanat.* 2017;11:71.
 64. Cruz-Martín A, El-Danaf RN, Osakada F, Sriram B, Dhande OS, Nguyen PL, et al. A dedicated circuit links direction-selective retinal ganglion cells to the primary visual cortex. *Nature.* 2014;507:358–61.
 65. Barbas H, Pandya DN. Architecture and intrinsic connections of the prefrontal cortex in the rhesus monkey. *J Comp Neurol.* 1989;286:353–75.
 66. Manita S, Suzuki T, Homma C, Matsumoto T, Odagawa M, Yamada K, et al. A top-down cortical circuit for accurate sensory perception. *Neuron.* 2015;86:1304–16.
 67. Abs E, Poorthuis RB, Apelblat D, Muhammad K, Pardi MB, Enke L, et al. Learning-related plasticity in dendrite-targeting layer 1 interneurons. *Neuron.* 2018;100:684–99.e6.
 68. Huttenlocher PR. Synapse elimination and plasticity in developing human cerebral cortex. *Am J Ment Defic.* 1984;88:488–96.
 69. Südhof TC. The cell biology of synapse formation. *J Cell Biol.* 2021;220:e202103052.
 70. Hua JY, Smith SJ. Neural activity and the dynamics of central nervous system development. *Nat Neurosci.* 2004;7:327–32.
 71. Dalakas MC, Alexopoulos H, Spaeth PJ. Complement in neurological disorders and emerging complement-targeted therapeutics. *Nat Rev Neurol.* 2020;16:601–17.
 72. Matsuda T, Cepko CL. Electroporation and RNA interference in the rodent retina in vivo and in vitro. *Proc Natl Acad Sci USA.* 2004;101:16–22.
 73. Comer AL, Sriram B, Yen WW, Cruz-Martín A. A pipeline using bilateral in utero electroporation to interrogate genetic influences on rodent behavior. *J Vis Exp.* 2020:e61350. <https://doi.org/10.3791/61350>.
 74. dal Maschio M, Ghezzi D, Bony G, Alabastri A, Deidda G, Brondi M, et al. High-performance and site-directed in utero electroporation by a triple-electrode probe. *Nat Commun.* 2012;3:960.
 75. Beaudoin GMJ, Lee S-H, Singh D, Yuan Y, Ng Y-G, Reichardt LF, et al. Culturing pyramidal neurons from the early postnatal mouse hippocampus and cortex. *Nat Protoc.* 2012;7:1741–54.
 76. Cole RW, Jinadasa T, Brown CM. Measuring and interpreting point spread functions to determine confocal microscope resolution and ensure quality control. *Nat Protoc.* 2011;6:1929–41.
 77. Stevens B, Johnson MB. The complement cascade repurposed in the brain. *Nat Rev Immunol.* 2021;21:624–5.

ACKNOWLEDGEMENTS

We thank Drs. Thomas Gilmore, J. Tiago Gonçalves, Angela Ho, Ashley Comer, and members of the Cruz-Martín lab for critical reading of the manuscript and helpful discussions. We want to thank Dr. Michael Kirber and the Med Campus Cellular Imaging Core for providing support with STED experiments and Dr. Todd Blute and the Boston University Biology Imaging Core for providing support for the confocal microscope.

AUTHOR CONTRIBUTIONS

RAP and AC-M conceptualized experiments including formulating composition, goals, and scope of the paper and approaches for analyses. RAP, EK, LAF, AB, MS, IP, CJ, CY, BEV and YYL collected the data and performed experiments. RAP, EK and LAF performed data curation. RAP, EK, LAF, AB, IP and DS analyzed data. RAP and LAF contributed code for data analysis. RAP, AC-M, EK, LAF, AB and MS contributed to parts of the original draft, including figure design and generation. All authors contributed to revision and editing of the draft. AC-M obtained funding and supervised the project providing mentorship, oversight, and project administration.

FUNDING

This work was supported by a National Institutes of Health R01 (NIMH, 1R01MH129732-01) to AC-M; and a Brenton R. Lutz Award to RAP.

COMPETING INTERESTS

The authors declare no competing interests.

ADDITIONAL INFORMATION

Supplementary information The online version contains supplementary material available at <https://doi.org/10.1038/s41380-024-02701-7>.

Correspondence and requests for materials should be addressed to Alberto Cruz-Martín.

Reprints and permission information is available at <http://www.nature.com/reprints>

Publisher's note Springer Nature remains neutral with regard to jurisdictional claims in published maps and institutional affiliations.



Open Access This article is licensed under a Creative Commons Attribution-NonCommercial-NoDerivatives 4.0 International License, which permits any non-commercial use, sharing, distribution and reproduction in any medium or format, as long as you give appropriate credit to the original author(s) and the source, provide a link to the Creative Commons licence, and indicate if you modified the licensed material. You do not have permission under this licence to share adapted material derived from this article or parts of it. The images or other third party material in this article are included in the article's Creative Commons licence, unless indicated otherwise in a credit line to the material. If material is not included in the article's Creative Commons licence and your intended use is not permitted by statutory regulation or exceeds the permitted use, you will need to obtain permission directly from the copyright holder. To view a copy of this licence, visit <http://creativecommons.org/licenses/by-nc-nd/4.0/>.

© The Author(s) 2024